Three-dimensional analysis of subwavelength diffractive optical elements with the finite-difference time-domain method

Mark S. Mirotznik, Dennis W. Prather, Joseph N. Mait, William A. Beck, Shouyuan Shi, and Xiang Gao

We present a three-dimensional (3D) analysis of subwavelength diffractive optical elements (DOE's), using the finite-difference time-domain (FDTD) method. To this end we develop and apply efficient 3D FDTD methods that exploit DOE properties, such as symmetry. An axisymmetric method is validated experimentally and is used to validate the more general 3D method. Analyses of subwavelength gratings and lenses, both with and without rotational symmetry, are presented in addition to a 2×2 subwavelength focusing array generator. © 2000 Optical Society of America

OCIS codes: 050.1970, 000.4430.

1. Introduction

Diffractive optical elements (DOE's) with feature sizes smaller than the wavelength of illumination are referred to as subwavelength diffractive optical elements (SWDOE's). With incorporation of subwavelength features SWDOE's can be designed with significantly increased performance over their superwavelength counterparts. For example, in the case of binary structures, diffraction efficiencies in excess of 90% have been predicted[1] and efficiencies in excess of 80% have been measured experimentally.[2] However, this added performance is purchased at a significant cost. Namely, the analysis, and subsequent design, of SWDOE's requires the use of rigorous electromagnetic (EM) models. These models, which incorporate the full vector nature of EM fields, can be theoretically challenging to construct and often demand considerable computational resources.

Although the microwave community has put forth a considerable effort to develop computationally efficient EM algorithms, little of this research has been applied to optical devices such as SWDOE's. One exception is the large body of research on rigorous coupled-wave theory applied to the analysis and the design of infinitely periodic gratings with subwavelength features.[3] However, only a handful of these articles address finite aperiodic SWDOE's,[4–6] and these analyze only one-dimensional elements. To the best of the authors' knowledge, ours is the first application of a rigorous three-dimensional (3D) EM model to two-dimensional (2D) finite aperiodic SWDOE's.

Here we present the use of the finite-difference time-domain (FDTD) method for the analysis of 2D SWDOE's. We present the implementation of a full 3D FDTD as well as an axisymmetric implementation of the FDTD that can be applied to rotationally symmetric SWDOE's. We will show that the FDTD is a computationally practical method for performing 3D analysis on finite aperiodic SWDOE's. The methods are validated by comparison with analytical solutions and, in the case of the axisymmetric model, with experimental results. Specific examples are given for binary subwavelength lenses, a subwavelength grating, and a diffractive 2×2 subwavelength focusing array generator.

2. Finite-Difference Time-Domain Method

The FDTD method was first introduced by Yee in his 1966 seminal paper.[7] The method was later refined by Taflove[8] and others[9,10] and is now one of the most widely used numerical techniques for solving EM

M. S. Mirotznik is with the Department of Electrical Engineering and Computer Science, The Catholic University of America, Washington, D.C. 20064. D. W. Prather (dprather@ee.udel.edu), S. Shi, and X. Gao are with the Department of Electrical and Computer Engineering, University of Delaware, Newark, Delaware 19716. J. N. Mait and W. A. Beck are with the U.S. Army Research Laboratory, AMSRL-SE-EO, Adelphi, Maryland 20783.

Received 3 August 1999; revised manuscript received 6 January 2000.

0003-6935/00/172871-10$15.00/0

problems. There are several advantages of this method over frequency-domain techniques such as the finite-element method (FEM) and boundary integral methods. First, the method is a direct solution of Maxwell's time-domain equations. Consequently, it is a complete full-wave solution that contains no approximations that would prevent a correct solution from being reached. FEM and integral methods can be plagued by spurious nonphysical solutions. Second, the method is extremely general in the materials and geometries it can analyze. Structures that contain inhomogenous, lossy, or even anisotropic material properties can be easily handled. Last, and most importantly, the memory requirements of the FDTD are significantly less than those of other methods, which permits efficient analysis of electrically large scatterers. This is of particular importance for the analysis of many practical SWDOE's, since their size may extend over hundreds of wavelengths. The principal disadvantage of the classical implementation of FDTD is that all structures must conform to a Cartesian grid. Consequently, all curved surfaces must be modeled by a stair-step approximation, which can introduce errors into the results.

The FDTD method derives its name from a direct finite-difference approximation to Maxwell's time-dependent curl equations,

$$\frac{\partial \mathbf{H}}{\partial t} = -\frac{1}{\mu}\nabla \times \mathbf{E}, \qquad \frac{\partial \mathbf{E}}{\partial t} = -\frac{1}{\epsilon}\nabla \times \mathbf{H} - \frac{\sigma}{\epsilon}\mathbf{E}, \quad (1)$$

where boldface is used to represent a vector quantity.

In a 3D rectangular coordinate system these equations can be expanded into an equivalent system of six coupled scalar equations for all electric and magnetic field components,

$$\frac{\partial H_x}{\partial t} = \frac{1}{\mu}\left(\frac{\partial E_z}{\partial y} - \frac{\partial E_y}{\partial z}\right), \qquad \frac{\partial E_x}{\partial t} = \frac{1}{\epsilon}\left(\frac{\partial H_z}{\partial y} - \frac{\partial H_y}{\partial z} - \sigma E_x\right), \quad (2)$$

$$\frac{\partial H_y}{\partial t} = \frac{1}{\mu}\left(\frac{\partial E_x}{\partial z} - \frac{\partial E_z}{\partial x}\right), \qquad \frac{\partial E_y}{\partial t} = \frac{1}{\epsilon}\left(\frac{\partial H_x}{\partial z} - \frac{\partial H_z}{\partial x} - \sigma E_y\right), \quad (3)$$

$$\frac{\partial H_z}{\partial t} = \frac{1}{\mu}\left(\frac{\partial E_y}{\partial x} - \frac{\partial E_x}{\partial y}\right), \qquad \frac{\partial E_z}{\partial t} = \frac{1}{\epsilon}\left(\frac{\partial H_y}{\partial x} - \frac{\partial H_x}{\partial y} - \sigma E_z\right). \quad (4)$$

Yee's basic scheme is to use a series of finite-difference approximations to transform Eqs. (2)–(4) into a system of six algebraic equations. These equations can then be solved with a simple leap-frog algorithm. For a detailed description and derivation of the full 3D FDTD equations the reader is referred to Ref. 8. For illustration we provide here the FDTD approximation for the E_x field component,

$$\begin{aligned} E_x|_{i,j,k}^{n+1} = {} & \frac{1 - \sigma_{i,j,k}\Delta t/2\epsilon_{i,j,k}}{1 + \sigma_{i,j,k}\Delta t/2\epsilon_{i,j,k}} E_x|_{i,j,k}^{n} \\ & + \frac{\Delta t/\epsilon_{i,j,k}}{1 + \sigma_{i,j,k}\Delta t/2\epsilon_{i,j,k}} \frac{1}{\Delta y}\left(H_z|_{i,j+1/2,k}^{n+1/2} - H_z|_{i,j-1/2,k}^{n+1/2}\right) \\ & - \frac{\Delta t/\epsilon_{i,j,k}}{1 + \sigma_{i,j,k}\Delta t/2\epsilon_{i,j,k}} \frac{1}{\Delta z}\left(H_y|_{i,j,k+1/2}^{n+1/2}\right. \\ & \left. - H_y|_{i,j,k-1/2}^{n+1/2}\right), \end{aligned} \quad (5)$$

where i, j, and k indices represent the x, y, and z spatial locations, respectively; n indicates the current time index; Δy and Δz represent the y and the z spatial increments, respectively; ϵ, σ, and μ represent the permittivity, electric conductivity, and magnetic permeability, respectively; and Δt is the time step. The unknown field distribution over a finite space is calculated by application of the six FDTD equations to a volumetrically sampled grid of cells called Yee cells. Each edge of a Yee cell may be assigned independent electrical properties, which allows one to model complex objects that can consist of lossy, inhomogenous, or anisotropic materials. Figure 1 illustrates how the field components are assigned to a unit Yee cell. We should note that the ½ time-step values, used in the n + ½ terms in Eq. (5), denote the sequential order of the FDTD computations. For instance, in Eq. (5) the magnetic field, at the n + ½ time step, was determined with the electric field value at the previous nth time step. In turn this magnetic field value is now being used to determine the electric field at the current time value, n + 1. This leap-frog process is continued until the FDTD computations are complete. This algorithm is generally referred to as the Yee, or time-marching, algorithm.

At t = 0 a plane-wave source of frequency f is assumed to be turned on. Solving the finite-difference equations at all lattice points simulates the propagation of waves from this source. Time stepping continues until the field components at each lattice point reach sinusoidal steady state. Alternatively, nonsinusoidal incident fields that contain an entire band of frequencies (e.g., Gaussian-modulated sinusoids) can be applied. When structures composed of only linear materials are analyzed, the various frequencies of the incident field propagate independently through the FDTD solution space. Therefore application of a Fourier transform to the time-dependent fields at each point in the solution space yields the steady-state field solution throughout the entire frequency spectrum of the incident field. In other words, we can obtain DOE performance over an entire spectrum of wavelengths in a single FDTD run.

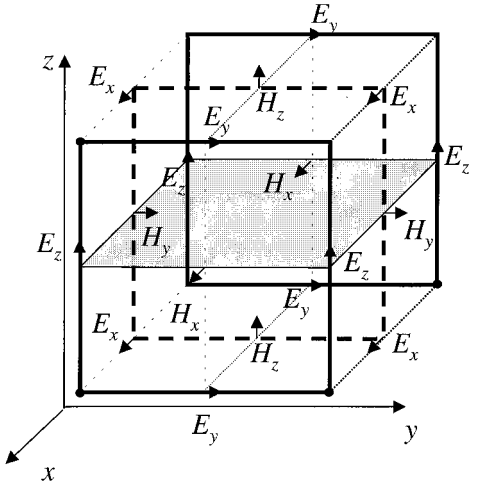

(a)

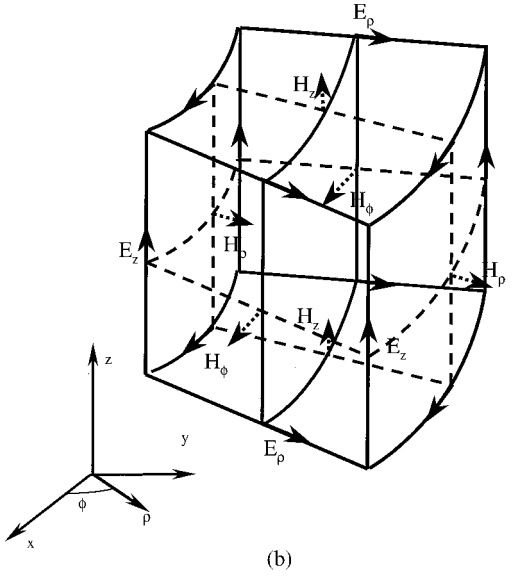

(b)

Fig. 1. Position of electric and magnetic field components about unit Yee cell in rectangular and polar coordinates.

3. Axisymmetric Finite-Difference Time-Domain

In the formulation of a diffraction model one should try, whenever possible, to exploit symmetries within the structure that improve computational efficiency. Such is the case for DOE's that contain axial symmetry, such as lenses and mode-shaping elements. In these cases Maxwell's equations can be represented in cylindrical coordinates where the azimuthal dependence can be expressed in terms of a Fourier series expansion in ϕ,

$$\mathbf{E}(\rho, \phi, z, t) = \sum_{k=1}^{\infty} E1_k(\rho, z, t)\cos(k\phi) + E2_k(\rho, z, t)\sin(k\phi), \quad (6)$$

$$\mathbf{H}(\rho, \phi, z, t) = \sum_{k=1}^{\infty} H1_k(\rho, z, t)\cos(k\phi) + H2_k(\rho, z, t)\sin(k\phi), \quad (7)$$

where the Fourier coefficients, $E1$, $E2$, $H1$, and $H2$, are determined by use of the FDTD method, as shown below. The resulting angular dependence can be factored out of Maxwell's equations so that the EM fields for each Fourier mode can be solved independently. The resulting form of Maxwell's curl equations, for the case of an incident field confined to the x, z plane, can be expressed as

$$\begin{aligned}
\mu \frac{\partial H_{\rho,k}}{\partial t} &= \frac{k}{\rho} E_{z,k} + \frac{\partial E_{\phi,k}}{\partial z}, \\
\mu \frac{\partial H_{\phi,k}}{\partial t} &= -\frac{\partial E_{\rho,k}}{\partial z} + \frac{\partial E_{z,k}}{\partial \rho}, \\
\mu \frac{\partial H_{z,k}}{\partial t} &= -\frac{1}{\rho}\frac{\partial(\rho E_{\phi,k})}{\partial \rho} - \frac{k}{\rho} E_{\rho,k}, \qquad (8) \\
\epsilon \frac{\partial E_{\rho,k}}{\partial t} &= -\frac{k}{\rho} H_{z,k} - \frac{\partial H_{\phi,k}}{\partial z} + \sigma E_{\rho,k}, \\
\epsilon \frac{\partial E_{\phi,k}}{\partial t} &= \frac{\partial H_{\rho,k}}{\partial z} - \frac{\partial H_{z,k}}{\partial \rho} + \sigma E_{\phi,k}, \\
\epsilon \frac{\partial E_{z,k}}{\partial t} &= \frac{1}{\rho}\frac{\partial(\rho H_{\phi,k})}{\partial \rho} - \frac{k}{\rho} H_{\rho,k} + \sigma E_{z,k}. \qquad (9)
\end{aligned}$$

Application of the FDTD method to the above equations results in a set of six coupled difference equations, which are shown below for the magnetic field components only,[8,11–13]

$$H^n_{\rho,k}(i,j) = H^{n-1}_{\rho,k}(i,j) + \frac{k\Delta t}{\mu\rho_0(i)} E^{n-1/2}_{z,k}(i,j) + \frac{\Delta t}{\mu\Delta z}[E^{n-1/2}_{\phi,k}(i,j+1) - E^{n-1/2}_{\phi,k}(i,j)], \quad (10)$$

$$H^n_{\phi,k}(i,j) = H^{n-1}_{\phi,k}(i,j) - \frac{k\Delta t}{\mu\Delta z}[E^{n-1/2}_{\rho,k}(i,j+1) - E^{n-1/2}_{\rho,k}(i,j)] + \frac{\Delta t}{\mu\Delta\rho}[E^{n-1/2}_{z,k}(i+1,j) - E^{n-1/2}_{z,k}(i,j)], \quad (11)$$

$$H^n_{z,k}(i,j) = H^{n-1}_{z,k}(i,j) - \frac{k\Delta t}{\mu\rho(i)} E^{n-1/2}_{\rho,k}(i,j) - \frac{\Delta t}{\mu\Delta\rho\rho(i)}[\rho_0(i+1)E^{n-1/2}_{\phi,k}(i+1,j) - \rho_0(i)E^{n-1/2}_{\phi,k}(i,j)], \quad (12)$$

where $\rho_0(i) = (i-1)\Delta\rho$, $\Delta\rho$, Δz are discretization lengths in ρ and z directions, respectively, and are shown in Fig. 1 and Δt is the time step.

4. Implementation

Custom programs that implement the FDTD method described above were written in Fortran 90 and run on a variety of computers ranging from personal com-

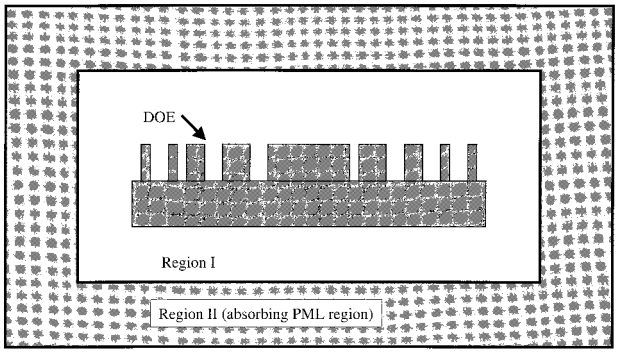

Fig. 2. Illustration of DOE located within FDTD solution space and absorbing PML region.

puters to high-performance Sun workstations. To reduce the computational demand of the FDTD method, it is advantageous to truncate the solution space as close to the scattering object as possible without introducing nonphysical reflections. To accomplish this, we constructed an absorbing boundary condition (denoted as region II in Fig. 2) that simulates an infinite free-space region surrounding the DOE. These boundary conditions effectively simulate an open infinite space by absorbing all outwardly propagating energy. We implemented absorbing boundary conditions, using the perfectly matched layer (PML) technique originally developed by Berenger.[14] The PML technique has been shown by several investigators to approximate an ideal absorbing boundary more closely than any previously developed absorbing boundary conditions.[15] The PML boundary condition is implemented by means of surrounding the FDTD space by absorbing layers of Yee cells that combine anisotropic electric and magnetic conductivity properties. Berenger found it possible to quickly attenuate waves entering the PML region while simultaneously matching the wave impedance at any angle of incidence (i.e., nearly zero reflectance). Conceptually, PML boundary conditions can be thought of as a numerical implementation of an anechoic chamber. We found that we could achieve reflection coefficients below 10^{-6} by applying 12–16 PML layers.

Table 1. Memory Requirements of Four of The Most Common Numerical Techniques in EM[a]

	Memory Requirements[b]	Example[c] $20 \times 20 \times 5\lambda^3$ Solution Space Estimated Memory Requirements
FDTD	Order N	64 Mbytes
FEM	Order $N \log N$	400 Mbytes
Volume integral methods	Order N^3	400 Gbytes
Boundary integral methods	Order N_b^3	15 Gbytes

[a] A sampling rate of ten samples per wavelength was assumed for these calculations.
[b] N, number of volume samples; N_b, number of boundary samples.
[c] $20\lambda \times 20\lambda \times 5\lambda$ solution space estimated memory requirements.

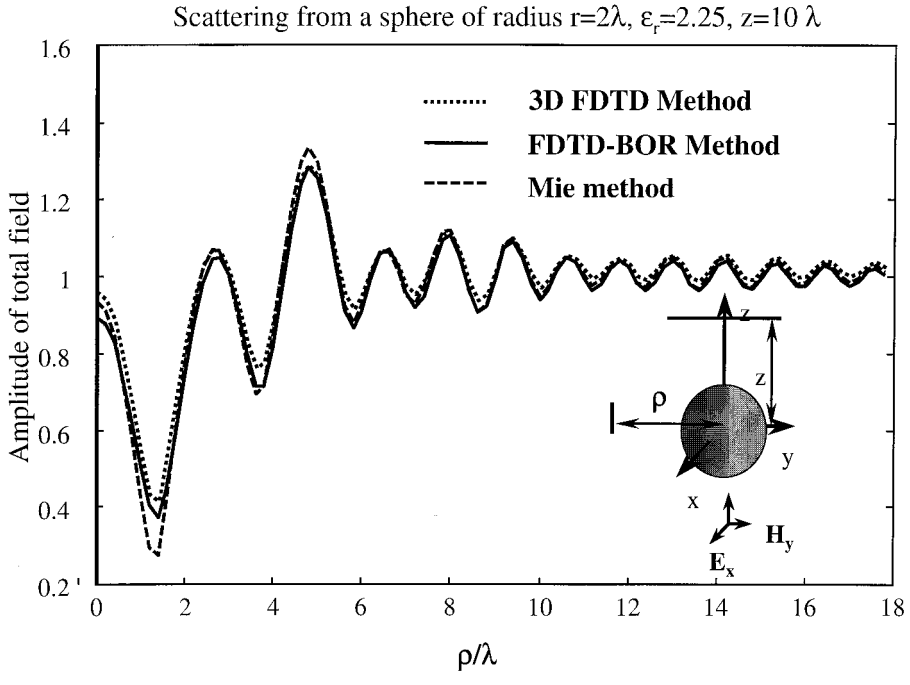

Fig. 3. Plane-wave scattering from dielectric sphere with a dielectric constant $\epsilon_r = 2.25$ and a radius of two free-space wavelengths, $2\lambda_0$, in size. Comparison of general 3D and axisymmetric FDTD codes with analytical solution. Plane-wave scattering from dielectric sphere with a dielectric constant $\epsilon_r = 2.25$ and a radius of two free-space wavelengths, $2\lambda_0$, in size. Comparison of general 3D and axisymmetric FDTD codes with analytical solution. BOR, boundary of revolution.

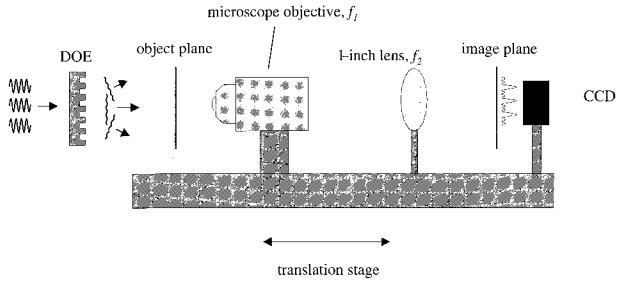

Fig. 4. Experimental setup for validating the axisymmetric FDTD formulation.

5. Computational Demand

One of the principal benefits of the FDTD method for the analysis of SWDOE's as compared with other popular techniques is its relatively low memory requirement. Table 1 illustrates the memory requirements of four of the most common numerical techniques in computational EM. The table also provides memory estimates for an example problem $20 \times 20 \times 5\ \lambda^3$ in size. It is clear from the table that for the analysis of electrically large objects (i.e., many wavelengths in size) the FDTD requires far less memory than the FEM or integral-based techniques. Since most practical SWDOE's fall into this class of electrically large problems, the FDTD provides in many cases the only practical approach.

It is difficult to quantify the computational time required by the FDTD method, since the time to reach steady state depends critically on the problem being solved. For example, highly resonant structures may require excessively long periods of time to reach steady state in the time domain.

6. Propagation Model

As mentioned above, to minimize both memory requirements and execution time, it is advantageous to truncate the FDTD solution space as close to the scattering object as possible. However, for many SWDOE's, the region of interest may be tens, hundreds, or even thousands of wavelengths away from the surface of the scatterer. One example is the focal plane of a diffractive lens. Since it is not computationally practical to extend the FDTD solution space to include these regions, we implemented a propagation model to handle this problem efficiently.

The propagation model begins by defining a closed surface within the FDTD solution space that completely surrounds the SWDOE. The FDTD method is used to calculate the steady-state magnitude and phase of both electric and magnetic field components along this surface. Using an exact propagation integral such as the Stratton–Chu formula, we then propagate these fields to any point outside the FDTD region. Specifically, the Stratton–Chu formula is written here as

$$\mathbf{E}(r) = \mathbf{E}_i(r) + \int_S \mathbf{E}_{sc} ds, \tag{13}$$

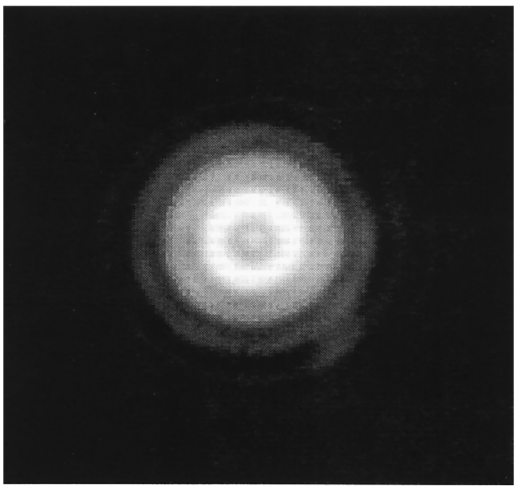

(a)

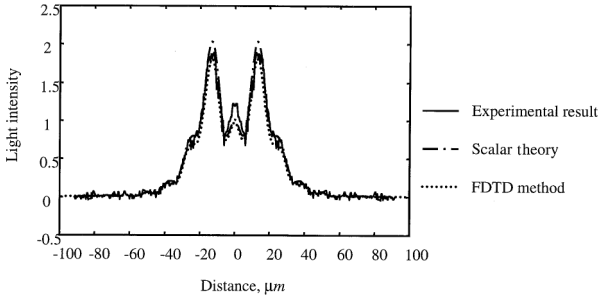

(b)

Fig. 5. Validation of the FDTD method by comparison of the measured and the computed values for a precision pinhole of 71 μm at an axial location of 1.2 mm.

where S is the defined surface; $\mathbf{E}_i$ is the incident field; and $\mathbf{E}_{sc}$ is given by

$$\mathbf{E}_{sc} = -j\omega\mu G(\hat{n} \times \mathbf{H}) - (\hat{n} \times \mathbf{E}) \times \nabla G - (\hat{n} \cdot \mathbf{E})\nabla G, \tag{14}$$

where $\hat{n}$ denotes the outward normal unit vector to the surface S, μ is the magnetic permeability, ω is the angular frequency, and G is the free-space Green's function given by

$$G(\mathbf{r} - \mathbf{r}') = \frac{1}{4\pi} \frac{\exp(-jk|\mathbf{r} - \mathbf{r}'|)}{|\mathbf{r} - \mathbf{r}'|}, \tag{15}$$

where k is the free-space wave number. When we implement Eqs. (13)–(15), the electric field at any point outside the defined surface can be calculated.

7. Validation

Two different methods were used to validate our FDTD codes. These are comparison with analytical solution for a dielectric sphere and comparison with experimental results; both are described below.

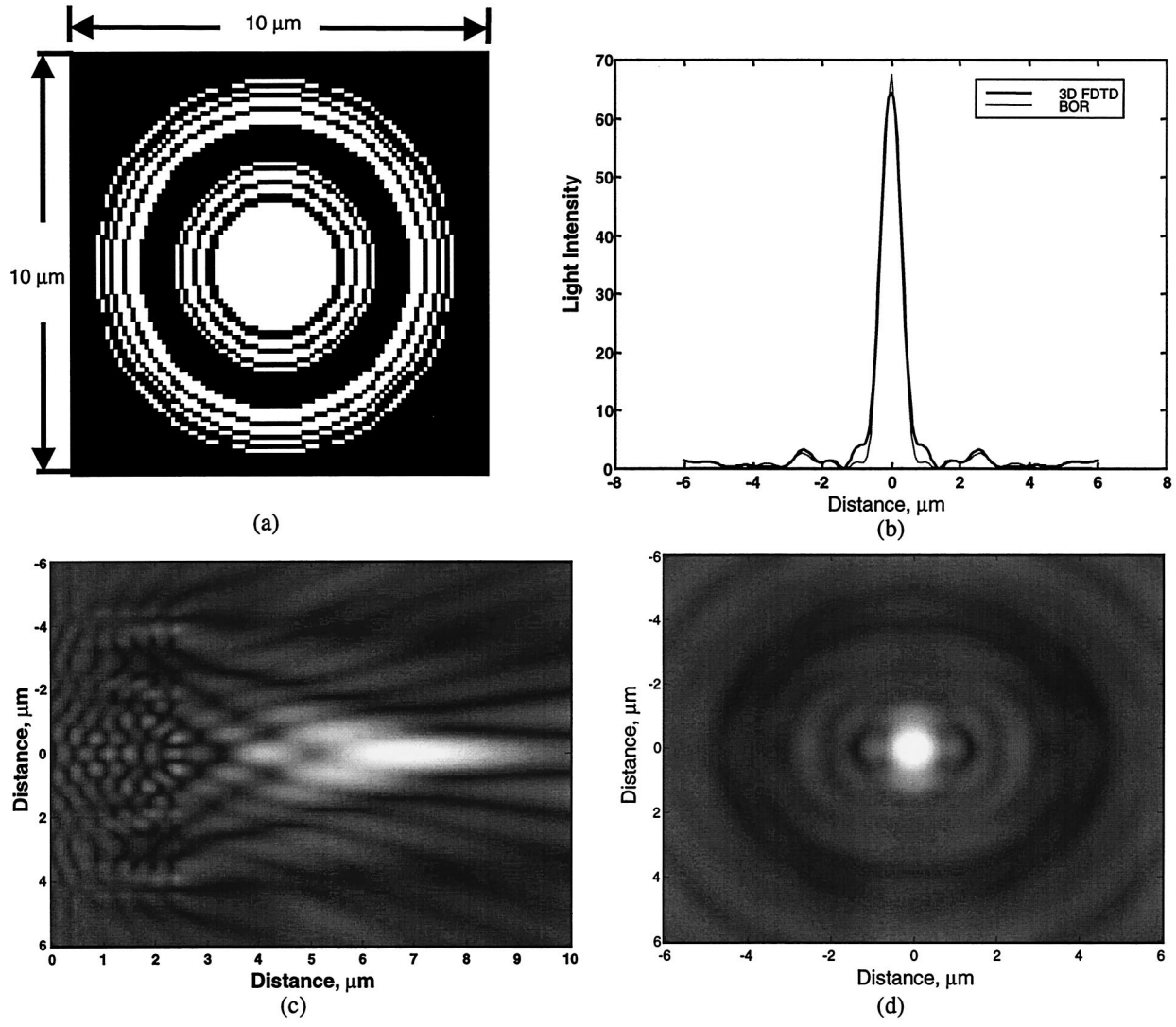

Fig. 6. Analysis of a subwavelength binary Fresnel zone plate: (a) lens profile, (b) line scans of the electric field intensities in the focal plane, (c) image plot of the electric field intensity in the x, z plane, and (d) image plot of the electric field intensity in the x, y focal plane. BOR, boundary of revolution.

A. Comparison with Analytical Solution

To test the accuracy of our FDTD code, we calculated the scattered fields from a dielectric sphere. The sphere was assigned a dielectric constant $\epsilon_r = 2.25$ and a radius of two free-space wavelengths, $2\lambda_0$, in size. The incident field was assumed to be a plane wave linearly polarized in the $\hat{x}$ direction and propagating in the positive $\hat{z}$ direction (see Fig. 3). A spatial sampling size of $\lambda_0/20$ was used in all FDTD simulations. The steady-state intensity of the total electric field was determined along a line $y = 0$ and $z = 10\lambda_0$ with the general 3D FDTD, the axially symmetric FDTD, and an exact analytical expression. The results, shown in Fig. 3, reveal a good agreement between the three methods to within an average percentage error of less than 3%. These small errors in the 3D FDTD results are most likely the consequence of modeling the smooth surface of a sphere with cubical elements. This staircase approximation to curved surfaces is one of the biggest limitations of the traditional FDTD method.

B. Experimental Validation

We also experimentally validated our axisymmetric FDTD model by constructing a micro-4f imaging system, based on a microscope objective (20×) and a 1-in.-diameter lens. The system has an overall magnification of 4.2 (based on the ratio of the two focal lengths, f_2/f_1) and was able to resolve 1-μm minimum features. The entire imaging system is mounted on an x, z translation stage, as shown in Fig. 4. Because the object and the image planes, in this system, are fixed and well defined, they can be used to determine the axial location relative to the DOE, i.e., the reference plane for where $z = 0$. This is achieved by translation of the imaging system toward the DOE until the surface is imaged onto the CCD. Subsequently, the translation stage, with the entire imag-

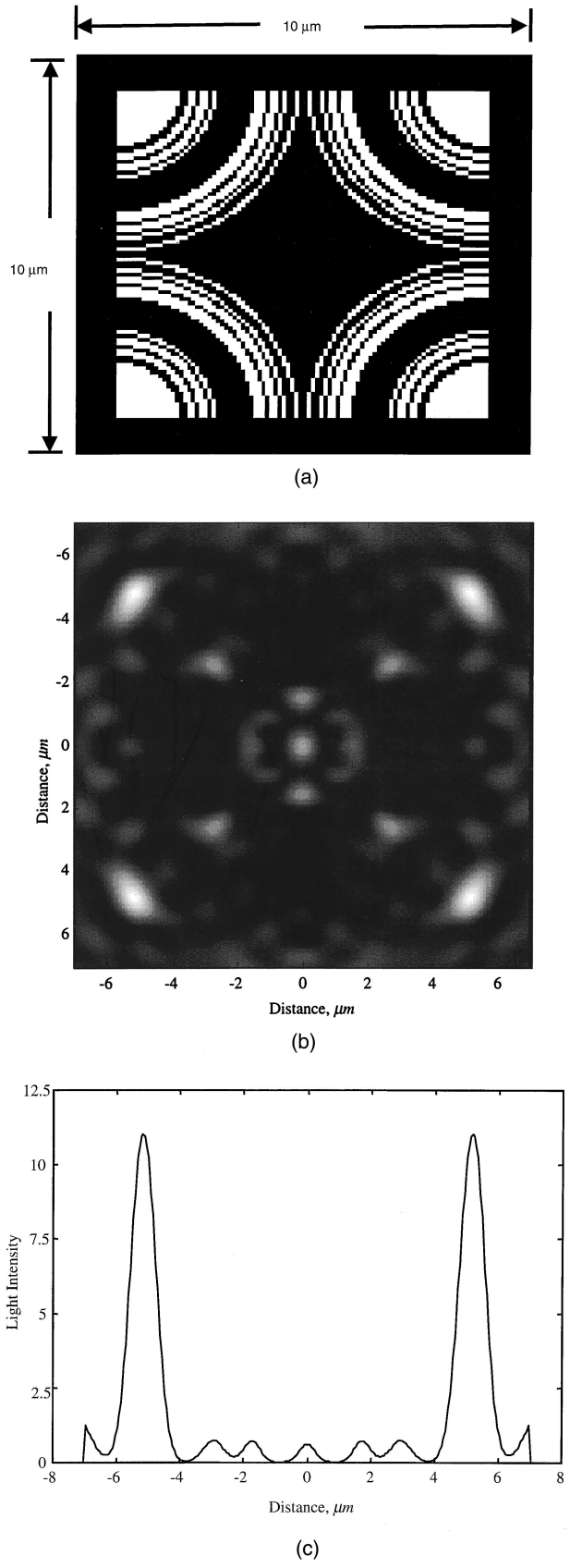

Fig. 7. Analysis of a 2 × 2 spot diffractive spot generator: (a) lens profile, (b) image plot of the electric field intensity in the x, y focal plane, and (c) line scans of the electric field magnitudes in the focal plane.

ing system on it, is translated back to the plane of interest, i.e., $z = z_0$. Because the microscope objectives have large numerical apertures, the performance of the imaging system, i.e., its modulation transfer function, reproduces the intensity profile in the object plane, i.e., the observation plane, with excellent fidelity.

To validate our FDTD model, we used the system to measure the diffracted light from a precision pinhole of 71 μm in diameter, from a collimated incident wave of 633 nm. We then calculated the diffracted light, using both scalar diffraction theory and the FDTD model. Results for $z = 1.2$ mm are shown in Fig. 5. The apparent agreement between the two is encouraging. Additional measurements were made along the z axis and showed similar agreement.

C. Examples

Our validation results gave us the confidence to apply our models to the analysis of several elements. To illustrate the FDTD method for the analysis of 2D SWDOE's, we analyzed two binary subwavelength diffractive lenses and a focusing diffractive 2 × 2 spot array. The elements were designed with a technique that combines scalar diffraction theory with effective medium theory.[16] In the present paper we extend this technique to two dimensions. All computations were performed on a 250-MHz Sun Ultra Sparc workstation running custom 3D FDTD code programmed in Fortran 90. Each of the FDTD meshes required approximately 5 million Yee cells, over 200 Mbytes of computer memory, and nearly 8 h of computation time.

D. Axisymmetric Diffractive Lens

A subwavelength binary Fresnel zone plate was designed and analyzed with the 3D FDTD method. All the diffractive lenses presented here were designed with a technique we developed that combines scalar diffraction and effective medium theory.[16] The lens was designed with a 5-μm focal length and a 10 μm × 10 μm aperture. Its minimum feature size was 0.1 μm. The wavelength of illumination in free space was 1.0 μm, and the index of refraction of the lens was 1.5. The binary features, illustrated by the white regions in Fig. 6(a), have an etch depth of 2 μm. The incident field was a normally incident plane wave of unit amplitude linearly polarized in the y direction. The lens was analyzed with a finite-difference grid of cubical cells 0.05 μm on a side (1/20 the free-space wavelength). The lens was surrounded by an absorbing boundary with 16 PML absorbing layers. To validate our calculations, we compared the 3D FDTD results with a boundary of revolution model, using the boundary element method. The results from the two models, shown in Fig. 6(b), clearly exhibit similar behavior with an average deviation of 3.5%. The diffraction efficiency of the lens was calculated to be 52%. The small discrepancies in the two calculations are most likely due to the FDTD approximation of a circular lens using cubical cells.

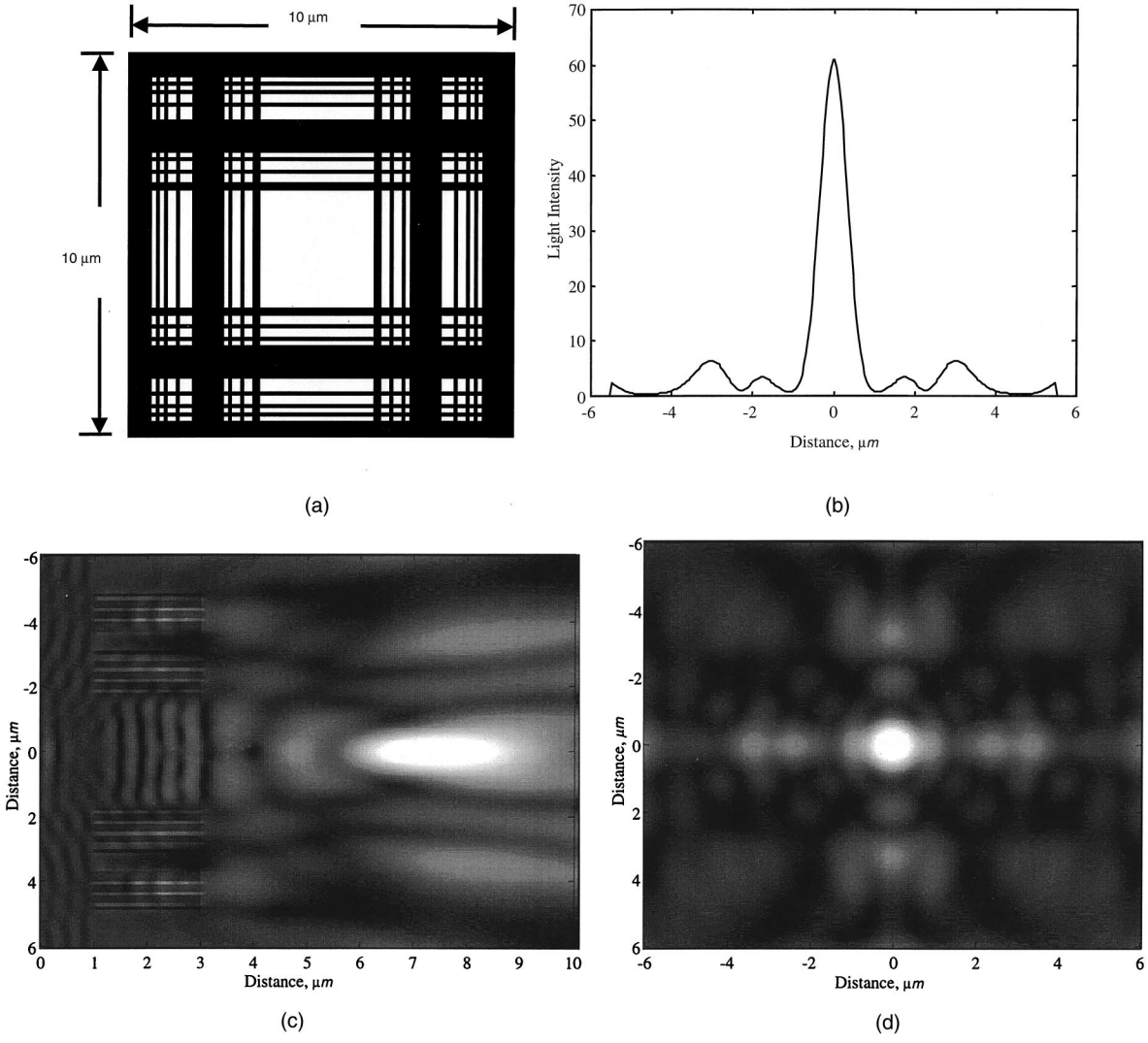

Fig. 8. Analysis of a nonaxisymmetric diffractive lens: (a) lens profile, (b) line scans of the electric field intensities in the focal plane, (c) image plot of the electric field intensity in the x, z plane, and (d) image plot of the electric field intensity in the x, y focal plane.

E. Focusing Array Generator

The diffractive lens described above possesses symmetries that allow for a more efficient analysis with an axisymmetric model. However, by translation and replication of the axisymmetric lens, a 2×2 spot array can be constructed that does not possess rotational symmetry. Consequently, a full 3D analysis is required. Here the focal length, aperture size, wavelength, incident field, and FDTD cell size are all the same as in the previous examples. The results shown in Fig. 7 reveal four focal spots located in the corners of the focal plane. One interesting observation is that the maximum light intensity in each of the focal spots is slightly less than 25% of the maximum light intensity of the axisymmetric lens shown in Fig. 6. This is not too surprising, since the sum of the efficiencies of each of the quarter lenses used in the array generator will likely be less efficient, owing to edge effects, than the efficiency of the whole lens.

F. Two-Dimensional Rectangular Lens

To further illustrate our ability to design and analyze fully 3D SWDOE's, we constructed the 2D separable rectangular lens illustrated in Fig. 8(a). The lens was designed with a 5-μm focal length and a 10 μm × 10 μm aperture. Its minimum feature size was 0.1 μm. The wavelength of illumination in free space was 1 μm, and the index of refraction of the lens was 1.5. The lens was analyzed with a finite-difference grid of cubical cells 0.05 μm on a side. The results of the analysis are shown in Figs. 8(b), 8(c), and 8(d). The diffraction efficiency of this lens was calculated to be 46%. With our design method it is possible to tailor the polarization behavior of separable lenses such as these.

G. Subwavelength Grating

As a final example a frequency-selective surface was designed and analyzed with the general 3D FDTD

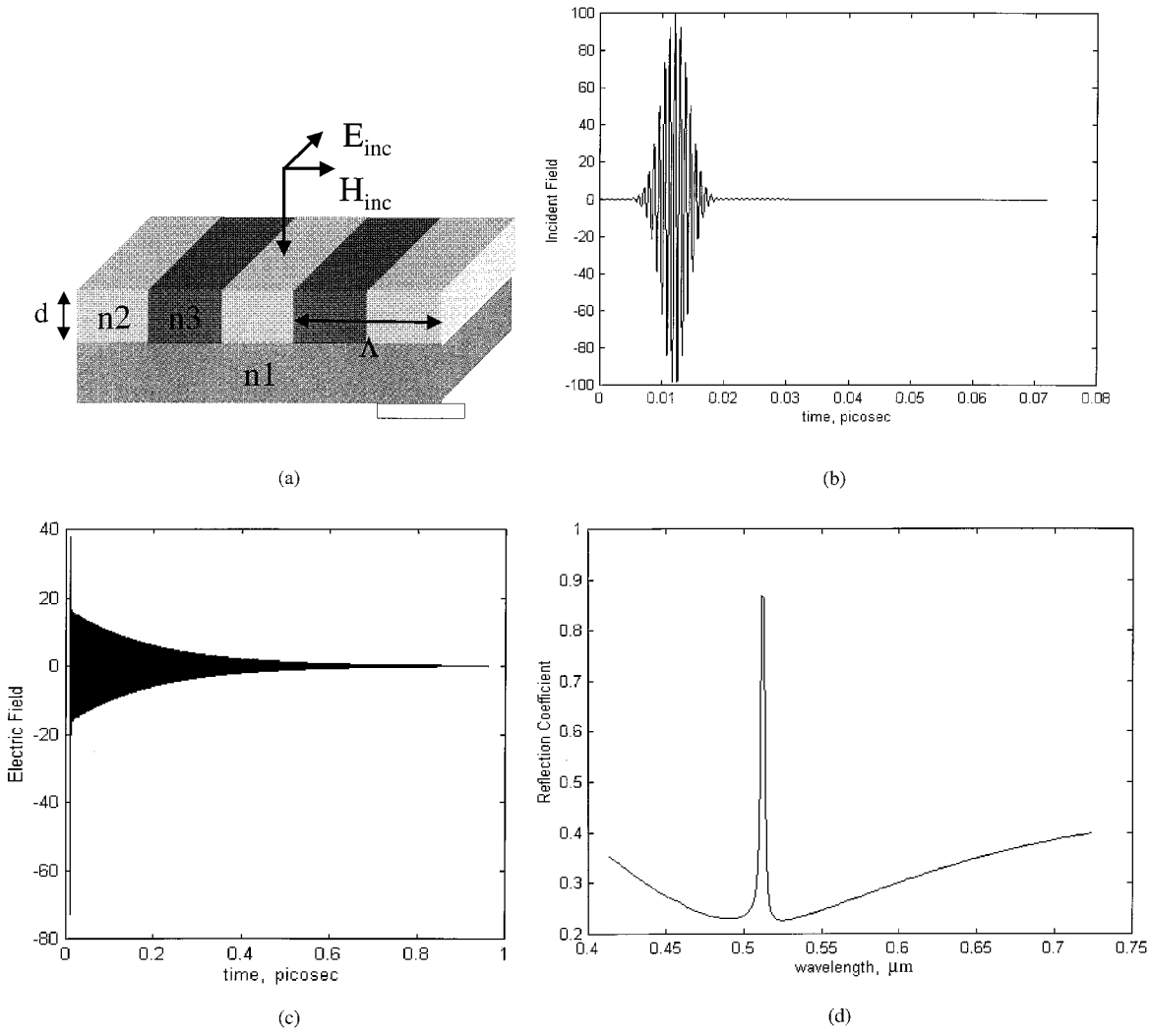

Fig. 9. Analysis of frequency-selective surface containing subwavelength infinite dielectric grating: (a) structure geometry, (b) electric field magnitude of incident field as a function of time, (c) electric field magnitude of reflected field as a function of time, and (d) frequency spectrum of reflection coefficient.

method. The design shown in Fig. 9(a) has an infinitely thick bottom substrate with index $n1 = 1.52$ covered by a subwavelength infinite grating of period $L = 0.3$ μm with indexes $n2 = 2.1$ and $n3 = 1.9$ and an etch depth of $d = 0.125$ μm. The incident field is assumed to be a normally incident plane wave polarized linearly in the y direction. The structure was designed to resonate at a wavelength of 0.51 μm with use of the method described by Tibuleac and Magnusson.[17] To simulate an infinitely periodic grating, we implemented periodic boundary conditions at $x = 0$ and $x = L$. The incident field, as shown in Fig. 9(b), is a pulse with a Gaussian-modulated temporal variation. The spectral content of the incident field is also Gaussian with a center wavelength of 0.51 μm and a bandwidth of 5.0 μm.

Figure 9(c) shows the time-domain response of the reflected field. It is interesting to note that significant reflected energy persists nearly a full picosecond after the incident field has died out. This is almost 1000 times the width of the incident pulse, clearly demonstrating the structure's highly resonant behavior. We should also note that because of this effect significant computation time could be required for analyzing highly resonant structures in the time domain. Figure 9(d) shows the frequency spectrum of the reflection coefficient, clearly revealing a narrow resonance peak at the designed center wavelength of 0.51 μm. This example illustrates the capability of FDTD to obtain a complete spectral response in a single run.

8. Conclusion

The finite-difference time-domain (FDTD) method was presented as an efficient means of performing three-dimensional (3D) analysis of SWDOE's. Custom code, using Fortran 90, was developed to permit analysis of both general 3D and axisymmetric diffractive optical elements (DOE's). The methods were validated analytically and experimentally. Specific examples of binary subwavelength lenses, subwavelength dielectric gratings, and a focused spot generator were provided to illustrate the usefulness of the

technique. Future research will concentrate on incorporating the codes in iterative design algorithms to perform 2D SWDOE synthesis.

References

1. M. W. Farn, "Binary gratings with increased efficiency," Appl. Opt. **31,** 4453–4458 (1992).
2. P. Lalanne, S. Astilean, P. Chavel, E. Cambril, and H. Launois, "Blazed-binary subwavelength gratings with efficiencies larger than those of conventional echelette gratings," Opt. Lett. **23,** 1081–1083 (1998).
3. T. K. Gaylord and M. G. Moharam, "Analysis and applications of optical diffraction by gratings," Proc. IEEE **73,** 894–937 (1985).
4. M. S. Mirotznik, D. W. Prather, and J. N. Mait, "A hybrid finite-boundary element method for the analysis of diffractive elements," J. Mod. Opt. **43,** 1309–1322 (1996).
5. D. W. Prather, M. S. Mirotznik, and J. N. Mait, "Boundary integral methods applied to the analysis of diffractive optical elements," J. Opt. Soc. Am. A **14,** 34–43 (1997).
6. K. Hirayama, E. N. Glytsis, T. K. Gaylord, and D. W. Wilson, "Rigorous electromagnetic analysis of diffractive cylindrical lenses," J. Opt. Soc. Am. A **13,** 2219–2231 (1996).
7. K. S. Yee, "Numerical solution of initial boundary value problems involving maxwell's equations in isotropic media," IEEE Trans. Antennas Propag. **AP-14,** 302–307 (1966).
8. A. Taflove, *Computational Electromagnetics: The Finite-Difference Time Domain Method* (Artech House, Boston, Mass., 1995).
9. R. Luebbers, R. F. Hunsberger, K. Kunz, R. Standler, and M. Schneider, "A frequency dependent finite-difference time-domain formulation for dispersive materials," IEEE Trans. Electromagn. Compat. **32,** 222–229 (1990).
10. K. S. Kunz and R. J. Luebbers, *The Finite Difference Time Domain Method for Electromagnetics* (CRC Press, Boca Raton, Fla., 1993).
11. D. Davidson and R. Ziolkowski, "Body-of-revolution finite-difference time-domain modeling of space-time focusing by a three-dimensional lens," J. Opt. Soc. Am. A **11,** 1471–1490 (1994).
12. Y. Chen, R. Mittra, and P. Harms, "Finite-difference time-domain algorithm for solving maxwell's equations in rotationally symmetric geometries," IEEE Trans. Microwave Theory Tech. **MTT-44,** 832–839 (1996).
13. D. W. Prather and S. Shi, "Formulation and application of the finite-difference time-domain method for the analysis of axially symmetric diffractive optical elements," J. Opt. Soc. Am. A **16,** 1131–1142 (1999).
14. J. P. Berenger, "A perfectly matched layer for the absorption of electromagnetic waves," J. Comput. Phys. **114,** 185–200 (1994).
15. D. S. Katz, E. T. Thiele, and A. Taflove, "Validation and extension to three dimensions of the berenger PML absorbing boundary condition for FD-TD meshes," IEEE Microwave Guid. Wave Lett. **4,** 268–270 (1994).
16. J. N. Mait, D. W. Prather, and M. S. Mirotznik, "Binary subwavelength diffractive-lens design," Opt. Lett. **31,** 1343–1345 (1998).
17. S. Tibuleac and R. Magnusson, "Reflection and transmission guided-mode resonance filters," J. Opt. Soc. Am. A **14,** 1617–1626 (1997).